



Superoxide radical induced redox processes for simultaneous reduction of Cr (VI) and oxidation of ciprofloxacin in wastewater

Kang Wang^{a,1}, Shuming Zeng^{b,1}, Geng Li^c, Yilin Dong^a, Qiuwen Wang^a, Lijun Zhang^a, Zhijun Ren^{a,*}, Pengfei Wang^{a,*}

^a School of Energy and Environmental Engineering, Hebei University of Technology, Tianjin 300401, China

^b College of Physics Science and Technology, Yangzhou University, Jiangsu 225009, China

^c National Supercomputer Center in Tianjin, Tianjin 300457, China



ARTICLE INFO

Keywords:
S-scheme photocatalyst
Superoxide radical
Simultaneous removal
Ciprofloxacin
Cr (VI)

ABSTRACT

Simultaneous removal of antibiotics and heavy metals from the wastewater is still a sophisticated task with great challenge. Interestingly, $\bullet\text{O}_2$ as a long-lived and highly active specie can simultaneously remove antibiotics and heavy metals. Herein, we design a S-type heterojunction photocatalyst, which can efficiently generate $\bullet\text{O}_2$. Characterizations and DFT calculation demonstrate that internal electric field provides powerful propulsion for migration of photo generated carriers between $\text{Zn}_{0.78}\text{Cd}_{0.22}\text{S}$ and $\text{g-C}_3\text{N}_4$, effectively extends electronic life, thereby enhances the production of $\bullet\text{O}_2$. Photocatalytic reaction rate constants under optimal composite ratio conditions were 3.1-times (ciprofloxacin) and 5.9-times (Cr (VI)) higher than $\text{Zn}_{0.78}\text{Cd}_{0.22}\text{S}$ under the coexisting pollutant system. Benefiting from the inbuilt electric field to stimulate electron transfer and utilization as well as the dual function of $\bullet\text{O}_2$, it reveals the possibility of practical wastewater treatment in the internal circulating fluidized bed reactor.

1. Introduction

Excessive emissions of various pollutants have caused serious environmental issues, particularly water pollution [1]. The variety of pollutants in actual water bodies have increased significantly, antibiotics and heavy metals as typical pollutants can enter the aquatic environment sequentially or simultaneously through multiple pathways, resulting in a combination of antibiotic and heavy metal pollution in water bodies [2–4]. Ciprofloxacin (CIP) as the most common class of antibiotics in emerging contaminants, is widely utilized in all aspects of medical, livestock and aquaculture industries, causing severe persistent toxicity and bacterial resistance [5]. In addition, Cr (VI) is considered one of the most hazardous heavy metal ions, giving rise to serious carcinogenicity [6]. Unfortunately, CIP and Cr (VI) coexistence in water bodies can induce bacteria to produce antibiotic resistance genes (ARGs) and heavy metal resistance genes (MRGs), which act as carriers of resistance genes that migrate along the food chain and ultimately threaten human health [7]. Due to the fact that CIP is often degraded by oxidation and Cr (VI) is removed by reduction, which makes the removal

of complex contamination more complex [8,9]. Therefore, it is urgent to investigate a method for the simultaneous removal of both contaminants.

Currently, for the removal of antibiotics and Cr (VI), a number of technologies have been developed, such as adsorption, membrane separation, biodegradation, etc. [10,11]. However, these traditional methods of simultaneous removal of compound pollution are time-consuming, inefficient and involve secondary contamination [12]. Photocatalysis technology has received considerable attention for its advantages in terms of environmental friendliness, abundant resources and sustainable development [13]. In the removal mechanism, photocatalysts can absorb photons to produce electrons (e^-) and holes (h^+) which can be used to reduce Cr (VI) and the oxidation of CIP [14]. However, due to the short life span of the e^- / h^+ pairs, the redox capacity has been limited. Fortunately, e^- / h^+ pairs by reacting with electron donors or acceptors adsorbed on catalyst surface to produce longer-lived and more efficient reactive oxygen species (ROS, e.g., $\bullet\text{OH}$, H_2O_2 and $\bullet\text{O}_2$) are considered to be an effective strategy for improving photocatalytic efficiency [15]. Among them, $\bullet\text{O}_2$ is regarded as an

* Corresponding authors.

E-mail addresses: renzhijun2003@126.com (Z. Ren), pengfeiwang@hebut.edu.cn (P. Wang).

¹ These authors contributed equally.

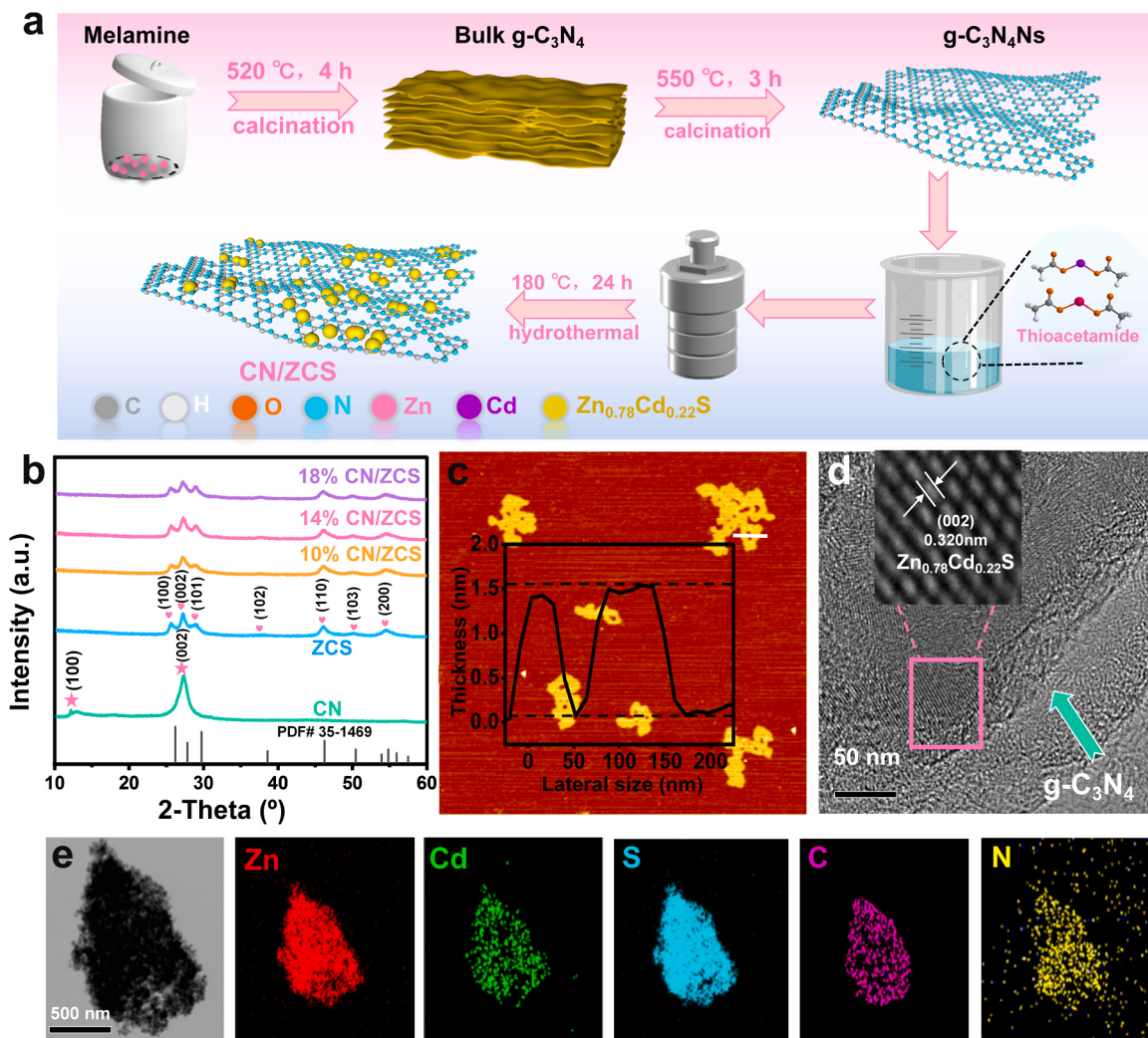


Fig. 1. (a) Schematic illustration of the fabrication process of CN/ZCS composite. (b) XRD patterns of CN, ZCS, and x% CN/ZCS, (c) AFM image of ultrathin CN nanosheet, TEM images of (d) 14 % CN/ZCS. (e) EDS elemental mappings of 14 % CN/ZCS.

excellent reactive species for the removal of complex contaminants due to the extremely long life span and the ability to simultaneously reduce heavy metals and oxidize organic pollutants [16]. Noteworthy, O₂ reduced by e⁻ is the main route to form •O₂. Therefore, it is essential to design and fabricate a photocatalyst with higher reduction potentials and longer electronic life.

Recently, the ternary metal sulfide (Zn_{0.78}Cd_{0.22}S) has gained much attention. On the one hand, sulphur is less electronegative, making it more conductive. On the other hand, the material has a suitable bandgap energy, which can absorb visible light and have applications in photocatalytic reactions. Unfortunately, due to the photo-corrosion and short lifetime of photo-generated electrons, further applications are hampered [17]. Excitingly, fabrication of Zn_{0.78}Cd_{0.22}S-based S-type photocatalysts is an effective strategy to effectively extend the photo-generated electron lifetime and help to mitigate photo-corrosion of the metal sulphides [18,19]. Graphitic carbon nitride (g-C₃N₄) as a metal-free material is visible-light active, harmless and has a fairly negative conduction band (CB) [20], which allows strong reduction capability of photogenerated electrons for the production of •O₂. Present day, effectively extended electronic life has been noted over some S-scheme nanocomposites that combine g-C₃N₄ with metal sulphides, for instance Co₃S₄ [21] and α-MnS [22], etc. However, few report shows the application of ternary solid solutions for composite contamination removal.

Here, we report a novel S-type heterojunction photocatalyst

consisting of Zn_{0.78}Cd_{0.22}S nanoparticles grown directly on g-C₃N₄ nanosheet for composite contamination removal. DFT calculation and characterizations indicate that construction of heterojunction accelerates the speed of electron transfer, extends the electron lifetime and produces more •O₂, which can improve photocatalytic performance. Consequently, 100 % of Cr (VI) and 88.6 % of CIP can be simultaneously removed within 20 min under visible light illumination. The simultaneous removal effect and recyclability in tap water bodies of photocatalyst for Cr (VI) and CIP were explored by an internal circulation fluidized bed photocatalytic reactor, which can still maintain a removal rate of over 70 % after 40 h of circulation.

2. Experimental

2.1. Chemicals and materials

All reagents are analytical grade and used without further purification treatment. Melamine and dehydrated acetic acid septum were both supplied by Komeo (Tianjin, China). zinc acetate provided by national pharmaceutical group (Shanghai, China). Mannitol was supplied by genuine leaf bio. (Shanghai, China), ciprofloxacin (CIP), thioacetamide, superoxide dismutase (SOD), K₂Cr₂O₇, ethylenediamine tetra acetic acid (EDTA-2Na) and silver nitrate (AgNO₃) were supplied by Macklin. (Shanghai, China).

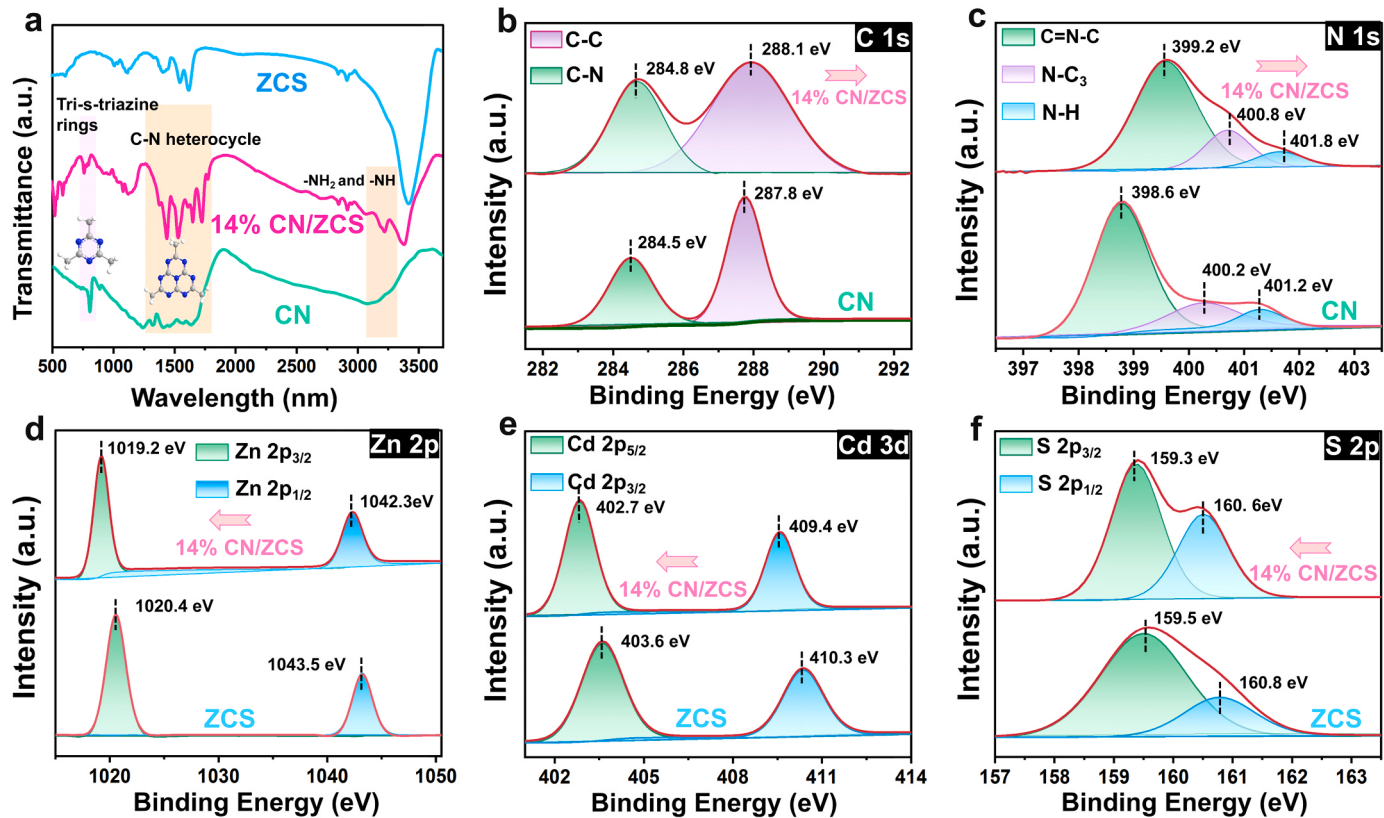


Fig. 2. (a) FTIR patterns of CN, ZCS and 14 % CN/ZCS composite. XPS core-level spectra of C 1 s (b), N 1 s (c), Zn 2 p (d), Cd 3 d (e), and S 2 p (f) states in CN, ZCS and 14 % CN/ZCS, respectively.

2.2. Preparation of samples

2.2.1. Preparation of ultrathin g-C₃N₄ nanosheet

Ultrathin g-C₃N₄ nanosheets (CN) were synthesized according to the paper with slightly modified [23]. Typically, melamine was utilized as the raw material and subjected to calcination at a temperature of 520 °C for a timeframe of 4 h, with an increment of 5 °C min⁻¹. The resulting bulk CN was then grinded into a powder with a mortar and subjected to an annealing process at 550 °C for 3 h to yield pale-yellow CN nanosheets. Subsequently, the CN was dispersed in isopropyl alcohol, and sonicated for 2 h. The yellow powder was separated via centrifugation and dried under vacuum at 50 °C for 6 h.

2.2.2. Preparation of g-C₃N₄/Zn_{0.78}Cd_{0.22}S heterojunction

Typically, a quantity of g-C₃N₄ nanosheets (CN) were sequentially added into 40 mL of deionized water, 30 min of ultrasound treatment, and then 1 mmol Zn (AC)₂ • 2 H₂O and Cd (AC)₂ • 2 H₂O were added to the suspension, kept stirring for 30 min. Afterwards, 10 mL of aqueous NaOH solution (0.4 M) was added vertically and slowly. Finally, added 2 mmol of thioacetamide to above solution and stirred for 20 min. The obtained solution was moved to a 100 mL autoclave, and then placed in an oven at 180 °C for a duration of 24 h. After the autoclave was cooled down to normal temperature the solids were collected by centrifugation after washing with anhydrous ethanol and DI water respectively, then dried under 60 °C all night. The obtained CN/ZCS composites with CN weight ratios of 10 wt%, 14 wt% and 18 wt% were symbolized as 10 % CN/ZCS, 14 % CN/ZCS and 18 % CN/ZCS, respectively. Pure Zn_{0.78}Cd_{0.22}S nanoparticles were prepared using the above method. No CN was added.

2.2.3. Preparation of photocatalyst loading on sponges

To load the photocatalyst onto the sponges, we have adopted the

following preparation method. First, 4.0 g 14 % CN/ZCS were dissolved in 40 mL C₂H₅OH to acquire a suspension, and 4 mL HNO₃ was added to the above suspension. Then, the homogeneous solution was heated to 80 °C for 30 min under ultrasound shock. Next, equal parts carrier sponges (1:1 vol ratio) were introduced to the previously dispersed 14 % CN/ZCS solution, ultrasonic was applied for 40 min. Finally, the sponges were dried at 60 °C, and the resulting sponge was labelled as CS. We show the detailed information of the carrier sponge in the support information (Fig. S1.).

2.3. Material characterizations and photocatalytic performance test

Details are provided in the Supporting information (Text S1 and Text S2).

2.4. Theoretical calculation and photoelectrochemical measurements

Information on theoretical calculation and photoelectrochemical measurements were provided in the Supporting information (Text S3 and Text S4).

3. Results and discussion

3.1. Morphology and structure of the photocatalysts

The synthesis procedure of g-C₃N₄/Zn_{0.78}Cd_{0.22}S is briefly summarized in Fig. 1a and g-C₃N₄/Zn_{0.78}Cd_{0.22}S was synthesized by calcination and hydrothermal. By tuning the amount of nanosheets, a range of catalysts with varying g-C₃N₄ contents were synthesized (denoted as x% g-C₃N₄/Zn_{0.78}Cd_{0.22}S, x delegates the mass percentage of g-C₃N₄). For convenience, g-C₃N₄, Zn_{0.78}Cd_{0.22}S, x% g-C₃N₄/Zn_{0.78}Cd_{0.22}S, are denoted as CN, ZCS, and x% CN/ZCS, respectively. The X-ray diffraction

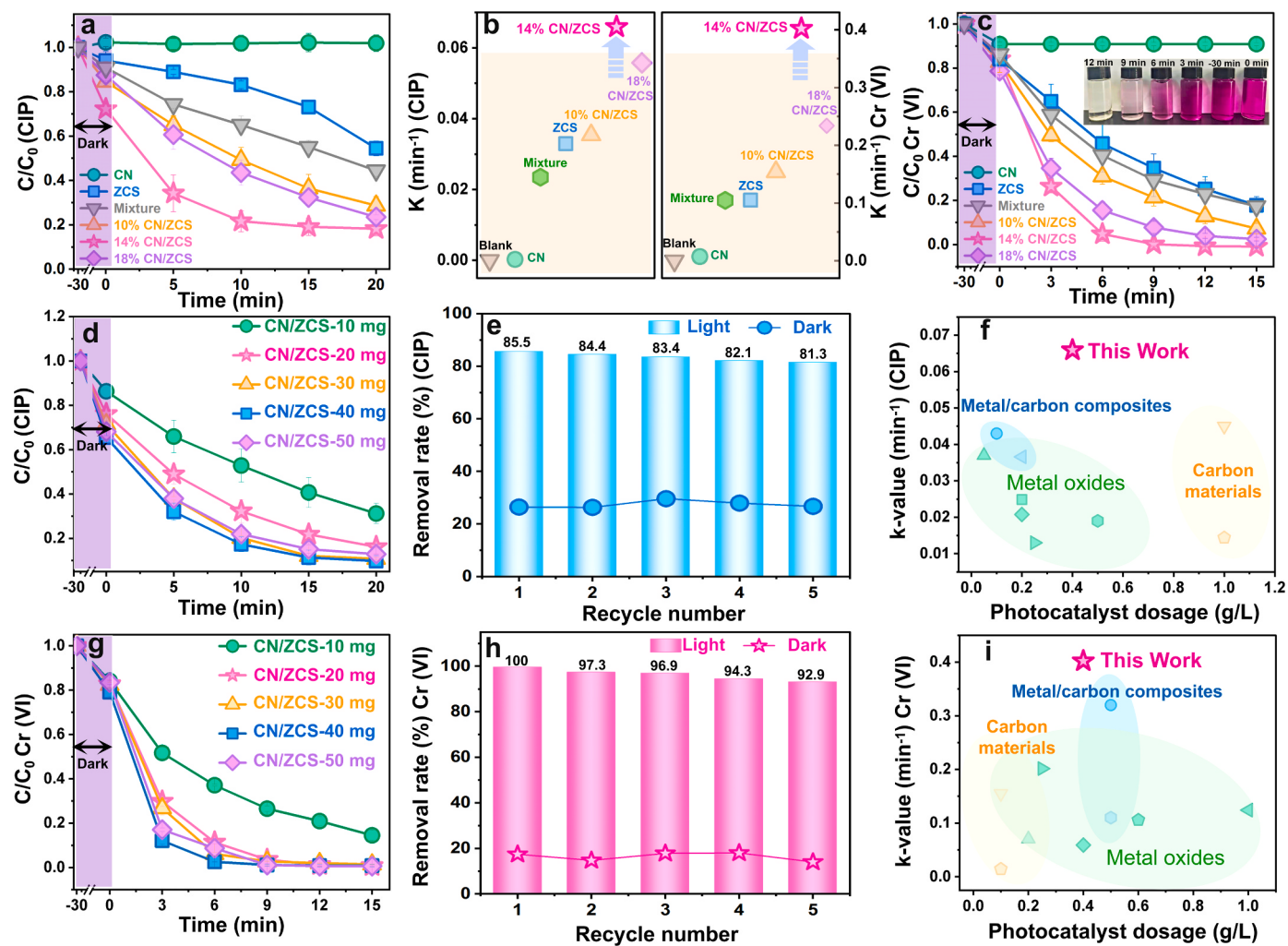


Fig. 3. (a) Photodegradation curves and (b) degradation kinetics of CIP (left). (c) Photoreduction curves and (b) reduction kinetics of Cr (VI) (right) by different samples. (d) Effects of dosage and (e) cycle stability of 14 % CN/ZCS on the degradation of CIP. (f) Comparison of k -values of the catalytic materials for the CIP degradation. (g) Effects of dosage and (h) cycle stability of 14 % CN/ZCS on the reduction of Cr (VI). (i) Comparison of k -values of the catalytic materials for the Cr (VI) reduction.

(XRD) and Brunauer-Emmett-Teller (BET) analysis expose structure and surface area of the catalysts (Fig. 1b, Fig. S2a,b and Table S1). The XRD patterns of the samples reveal a pure ZCS crystal phase (JCPDS No. 35-1469) and no obvious CN crystalline phase is observed, which indicate that the overlap of the CN (002) diffraction peak with ZCS (002) and its low crystallinity degree [24]. To intuitively confirm the presence of CN nanosheet in composite, atomic force microscopy (AFM) and transmission electron microscope (TEM) characterizations were carried out. CN exhibits an irregular porous lamellar structure with single layer thickness of roughly 1.5 nm (Fig. 1c and Fig. S3a), confirming its ultra-thin nanosheets structure. TEM images (Fig. S3b,c) reveal that ZCS consists of nanoparticles with an average size of 25 nm. After the combination, there are number of nanoparticles reside on the surface of CN nanosheet (Fig. 1d). Additionally, the high-resolution TEM (HRTEM) images (Fig. 1d inset) show that the lattice fringes of ZCS, while the lattice spacing of 0.168 nm is ascribed to the (101) crystal plane. The energy dispersive X-ray spectroscopy (EDX) elemental mapping images display that Zn, Cd, S, C, and N are uniformly distributed in CN/ZCS (Fig. 1e).

Fourier transform infrared (FTIR) spectroscopy was carried out to ascertain the surface functional groups and structures of the samples (Fig. 2a). For the pure CN, the absorption peaks at 807 cm^{-1} originates from the out-of-plane bending modes of tri-s-triazine rings and peaks at

$1200\text{--}1800\text{ cm}^{-1}$ are ascribed to the typical $\text{sp}^2\text{ C=N}$ and $\text{sp}^3\text{ C-N}$ bonds of the heptazine repeating units. The peaks located at $3000\text{--}3400\text{ cm}^{-1}$ are caused by surface amino vibrations, such as $-\text{NH}_2$ and $-\text{NH}$ [25]. In comparison, 14 % CN/ZCS at $1000\text{--}1700\text{ cm}^{-1}$ and $2700\text{--}3500\text{ cm}^{-1}$ show characteristic peaks similar to ZCS. In addition, the characteristic peaks of CN at 807 cm^{-1} , $1200\text{--}1800\text{ cm}^{-1}$ and $3000\text{--}3400\text{ cm}^{-1}$ can also be observed in 14 % CN/ZCS, which fully proves the successful combination of the two components [26].

X-ray photoelectron spectroscopy (XPS) was conducted to explore the interfacial interaction between CN and ZCS. The XPS survey spectrum (Fig. S4) discloses the existence of C, N, Zn, Cd, and S elements in 14 % CN/ZCS composite. C 1 s and N 1 s region of CN exhibit five typical peaks at 284.5, 287.8, 398.6, 400.2 eV, and 401.3 eV, corresponding to C-C and C-N species as well as $\text{C}=\text{N}-\text{C}$, $\text{N}-\text{C}_3$, and $\text{N}-\text{H}$ bonding, respectively (Fig. 2b and c). Compared with CN, 14 % CN/ZCS displays similar C 1 s and N 1 s spectra with five peaks, while these peaks present an obvious shift toward the direction of high binding energy. Zn 2p and S 2p region of ZCS form four typical peaks at 1024.4, 1043.5, 159.5, and 160.8 eV, corresponding to $\text{Zn }2p_{3/2}$ and $\text{Zn }2p_{1/2}$ states of Zn^{2+} as well as $\text{S }2p_{3/2}$ and $\text{S }2p_{1/2}$ states of S^{2-} , respectively. Importantly, after the combination of ZCS and CN, the peaks of Zn, Cd and S species shift toward the direction of low binding energy (Fig. 2d, e and f). Consequently, the above results reveal the tight integration and between CN

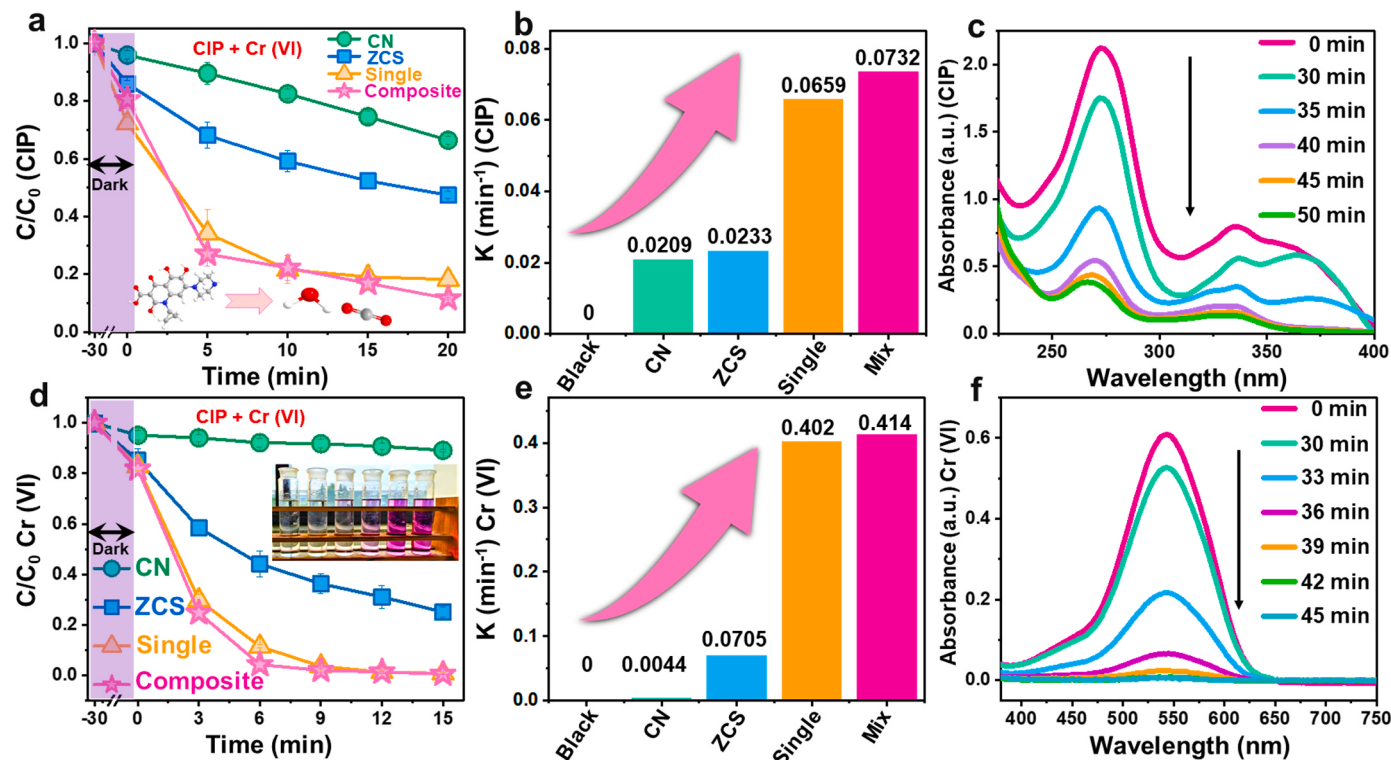


Fig. 4. (a) Photodegradation curves, (b) degradation kinetics of CIP in composite systems and (c) UV-vis absorbance spectra for 14 % CN/ZCS photocatalysts degradation of CIP in composite systems. (d) Photoreduction curves, (e) reduction kinetics of Cr (VI) and (f) UV-vis absorbance spectra for 14 % CN/ZCS photocatalysts Cr (VI) reduction in composite systems.

and ZCS existence of interfacial electron transfer, with the free electron migration from CN to ZCS. This charge redistribution between compounds may induce the formation of the internal electric field within CN/ZCS heterojunction [27].

3.2. The removal of CIP and Cr (VI) in the single and coexistence systems

To evaluate the photocatalytic reaction activity of samples in single system, the oxidative degradation of CIP and the reduction of Cr (VI) were picked as a reaction model. As depicted in Fig. 3a, as-prepared CN/ZCS composites show significantly increased removal capacity towards CIP. Wherein 14 % CN/ZCS achieves better CIP degradation (85.6 %). The first-order kinetic constants (k) of the CIP degradation attest that 14 % CN/ZCS has a higher k value (0.0659 min^{-1}), which is almost 2.3 times higher than ZCS (0.0293 min^{-1}) (Fig. 3b left). Subsequently, the reduction experiments of Cr (VI) were conducted. The reduction efficiency of Cr (VI) by 14 % CN/ZCS is evidently superior to ZCS, which can reach up to 99 % within 9 min (Fig. 3c). The reaction rate constant k of 14 % CN/ZCS reaches 0.402 min^{-1} , which is approximately 4 times as much as ZCS (0.103 min^{-1}) (Fig. 3b right). Noteworthy, CN and ZCS composite prepared by mechanical mixing does not display an enhanced photocatalytic activity, thus illustrating from one perspective the importance of heterojunction. Therefore, the representative sample of 14 % CN/ZCS with the best performance was selected. Fig. 3d and g exhibit the effects of various catalyst dosing levels on pollutant removal. Less or excessive amount of photocatalysts incurs deterioration photoactivity, which may be attributed to insufficient reactive sites or the presence of shielding impact and/or a catalyst agglomeration [28]. The 14 % CN/ZCS catalyst also exhibits superior reusability (Fig. 3e and h). In addition, the k -values of different catalytic systems for CIP degradation and reduction of Cr (VI) were calculated (Fig. 3f and i). Notably, the 14 % CN/ZCS exhibits the highest catalytic performance in the recently reported articles.

To further assess the performance of the photocatalysts,

photocatalytic reactions were conducted in the CIP and Cr (VI) coexistence system. In the absence of photocatalyst, the concentrations of CIP and Cr (VI) hardly change after 30 min of visible light exposure in the coexisting pollutant system, indicating that self-photolysis of CIP and Cr (VI) is insignificant (Fig. S5). Compared with the single pollutant systems, CIP and Cr (VI) removal efficiency are improved in the coexisting system. Taking 14 % CN/ZCS as the example, removal efficiency of CIP at single and coexisting system within 20 min are 85.6 % and 88.6 % (Fig. 4a). The kinetic constant of the coexisting pollutant system of CIP is calculated to be 0.0732 min^{-1} (Fig. 4b), which is improved compared with the single system (0.0659 min^{-1}). The Cr (VI) removal efficiency of single and coexisting system within 6 min are 90.3 % and 98.8 %, respectively (Fig. 4d). The kinetic constant of Cr (VI) in coexisting system is calculated to be 0.4135 min^{-1} (Fig. 4e), which is improved compared with the single system (0.402 min^{-1}). The UV-visible absorption spectrum also shows that the pollutants are removed and converted to other substances after the photocatalytic treatment (Fig. 4c, f). Noteworthy, 14 % CN/ZCS still exhibits excellent photocatalytic stability in composite systems (Figs. S6,7). From the above results, the photocatalytic removal efficiency increases when CIP and Cr (VI) were coexisted. The fact of this phenomenon can be ascribed to that CIP and Cr (VI) function as scavengers of the photoinduced holes and electrons, respectively, which can enhance the separation and utilization of holes and electrons and enhancing the photocatalytic performance.

3.3. Mechanisms of enhanced photocatalytic performance

To identify the major active species, the chemical quenching experiments were conducted (Fig. 5a). The removal rate of CIP degradation is significantly obstacle after the addition of disodium ethylenediaminetetraacetic acid (EDTA-2Na) and superoxide dismutase (SOD), implying that h^+ and $\bullet\text{O}_2$ play major roles in CIP degradation. Simultaneously, mannitol only slight inhibition in CIP degradation,

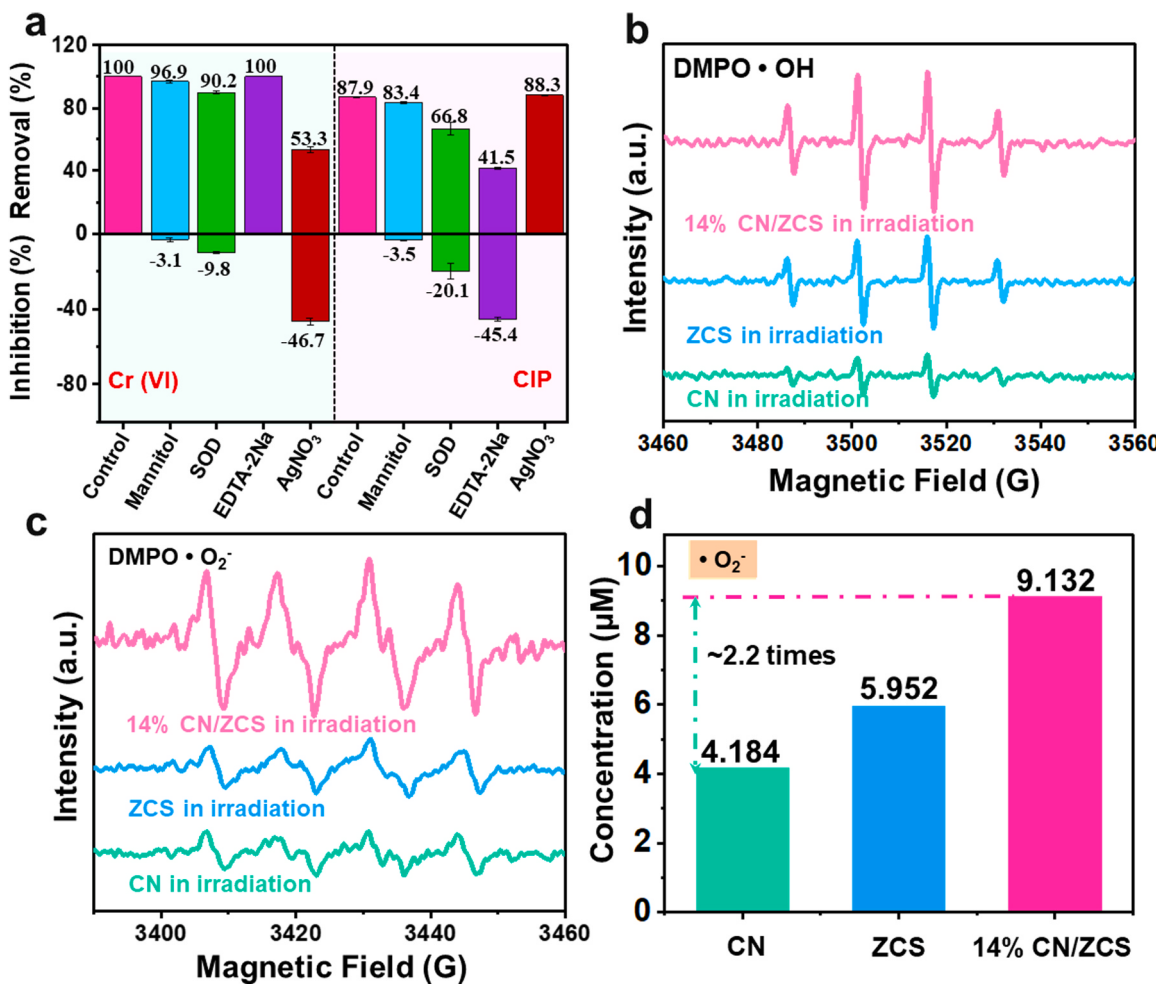


Fig. 5. (a) Comparison of removal performance of CIP and Cr (VI) under different quenchers conditions. EPR spectra of (b) DMPO-•OH and (c) DMPO-•O₂⁻. (d) Free radical quantification experiment of •O₂⁻.

implying that •OH slightly contributed to CIP degradation. With the addition of AgNO₃, the CIP degradation efficiencies are improved, it can be assigned to the fact that AgNO₃ acts as an electronic-trapping agent in the degradation system, which can hasten the separation of electron-hole pairs, ultimately promote the photodegradation of CIP. For the reduction of Cr (VI), the removal rate is significantly obstacle after addition of AgNO₃, implying that e⁻ plays a major role. Nevertheless, The addition of AgNO₃ cannot completely inhibit the removal of Cr(VI), because the reduction of Cr(VI) is also a process of capturing e⁻ [29]. Noteworthy, the reduction of Cr (VI) is inhibited after SOD was added. In addition, after addition the mannitol, the reduction of Cr (VI) is slightly inhibited suggesting that the production of •OH may have consumed a small number of •O₂⁻. From the above results, •O₂⁻ plays a role in both reduction and oxidation, which further justifying the strategy of extending the electron lifetime to generate more •O₂⁻ for the removal of complex pollution. The electron spin resonance (ESR) measurements were conducted to directly confirm the presence of active species. When 5,5-dimethyl-1-pyrroline-N-oxide (DMPO) is introduced into the reaction system, there was not any radical signal detected under dark conditions (Fig. S8), but four characteristic peaks of DMPO-•O₂⁻ radicals and DMPO-•OH radicals are inspected under the visible light irradiation. The characteristic peaks of •OH and •O₂⁻ are stronger for 14 % CN/ZCS than that of ZCS and CN (Fig. 5b and c). The radical quantitative testing was conducted to intuitively evidence that more radicals are produced. The concentration of •O₂⁻ is 9.132 μM for 14 % CN/ZCS, 2.2 times higher than CN for 4.184 μM (Fig. 5d) [30]. Additionally, the concentration of •OH also higher than CN (Fig. S9). In summary, the •O₂⁻ and •OH

radicals are considered to be reactive species and the construction of heterojunctions can effectively produce more reactive oxygen species [31].

To plumb the detailed interface charge transfer mechanism of the CN/ZCS heterojunction, electronic characteristics are calculated based on the constructed theoretical models as presented in Fig. 6 and Fig. S10. As indicated in Fig. 6a and b, CN emanates a higher work function (Φ) of 6.93 eV compared to ZCS ($\Phi = 4.61$ eV). Owing to the potential of Fermi energy (E_F) difference in specific orientations, when ZCS is tightly contacted with CN without illumination electrons at the interface will transfer from CN to ZCS until the equilibrium of E_F , which corresponds to the XPS results. To demonstrate more intuitively the existence of electron transfer between interfaces, the planar-averaged electron density was carried out (Fig. 6c and d). It is evident that charge redistribution occurs near the CN/ZCS interface. Blue and yellow regions on the constructed CN/ZCS model delegate that exhaustion and accumulation areas of electrons, respectively. These calculated results indicate that CN section near the interface is positively charged, while the ZCS region is negatively charged due to the electron migration. To determine the energy band structure of CN and ZCS, the photophysical and electrochemical experiments were carried out. Light absorption capacities of CN, ZCS and CN/ZCS heterojunctions were first evaluated using UV-visible diffuse reflectance spectroscopy (UV-Vis DRS) analysis. CN and ZCS show strong absorption bands with absorption margins at about 480 nm and about 518 nm, respectively (Fig. 6e). Essentially, the resulting CN/ZCS heterojunction exhibits enhanced and extended visible light absorption range compared to CN. Then, based on the

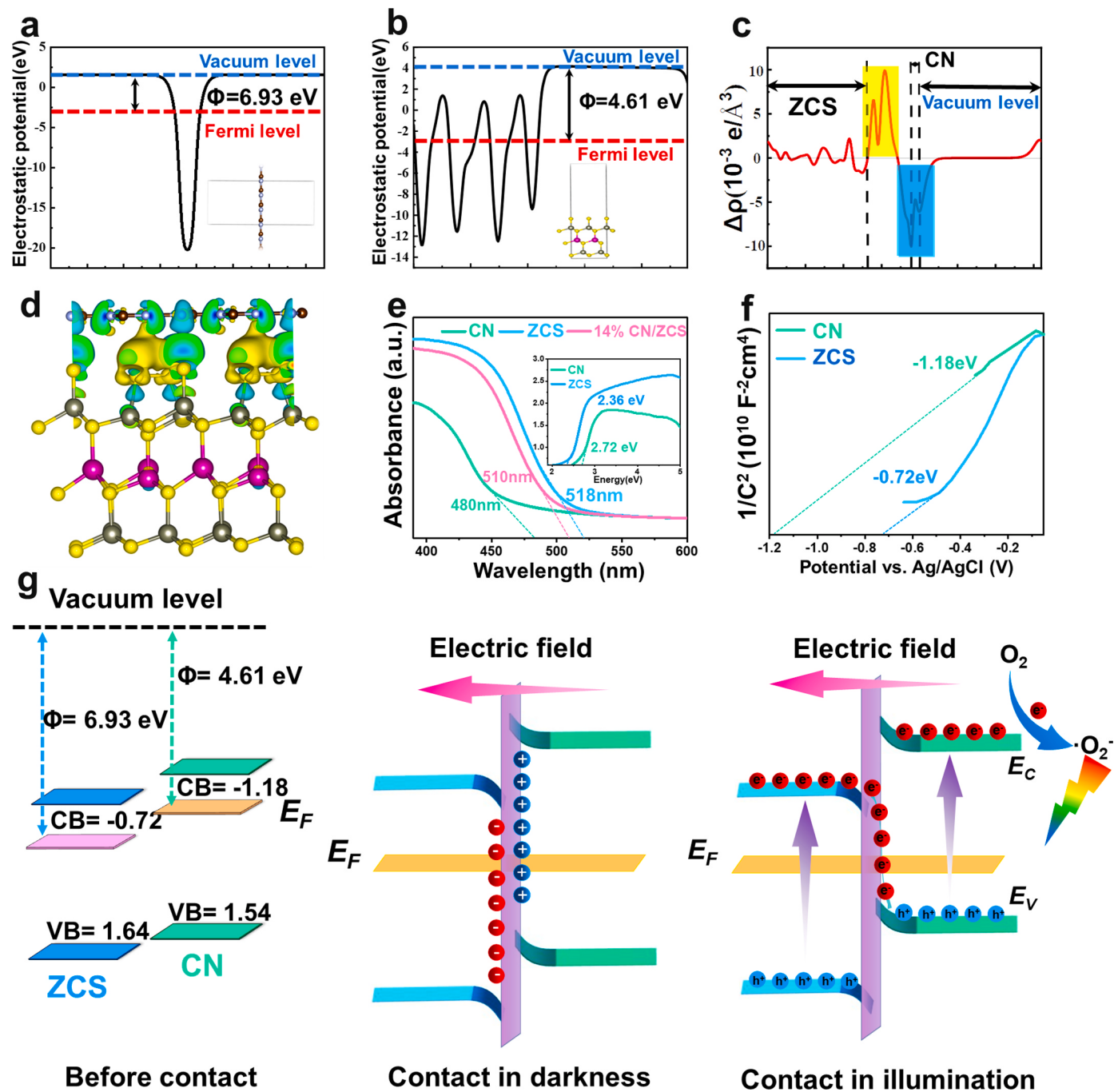


Fig. 6. The electrostatic potential and corresponding structural pattern of (a) CN and (b) ZCS, the insets are the models of the CN and ZCS for calculation, respectively. (c) The planar-averaged electron density difference and (d) side view of the charge density difference. (e) UV-vis spectra and with the inset showing the band gap energy (E_g) of CN and ZCS. Mott-Schottky plots for (f) CN and ZCS. (g) Charge transfer mechanism.

UV-vis DRS, bandgap (E_g) energies of the samples were acquired by the Kubelk-Munk method [32] (Fig. 6e, inset). The bandgaps of CN, and ZCS are determined to be 2.72 eV and 2.36 eV. The fermi energy level of a semiconductor can be evaluated by Mott-Schottky diagram. The flat band potentials of the CN and ZCS are calculated to be -1.18 eV and -0.72 eV versus NHE (pH 7) (Fig. 6f). Together, these data reveal the energy band energy structure of CN and ZCS. Based on the above results, a complete diagram of the electron transfer path is presented in Fig. 6g. An internal electric field is created due to the redistribution of electrons following contact between CN and ZCS. Under the light exposure, electrons receive photon energy and inspired to conduction band (CB). Then, the built-in electric field promotes the recombination of electrons

in CB of ZCS and holes in VB of CN, which can facilitate the separation of photogenerated electrons and holes while extending electronic lifetime and maintaining excellent oxidation and reduction capabilities. The above results provide sufficient evidence for the importance of the built-in electric field in S-type heterojunction.

Besides, charge separation and transfer efficiency are also two important factors affecting photochemical reactions. The extent of charge separation generated by absorption can be detected by the surface photovoltage (SPV) spectroscopy (Fig. 7a). It is confirmed that the SPV spectroscopy generated by 14 % CN/ZCS displays an apparent response range from 300 to 500 nm. Furthermore, the peak intensity of 14 % CN/ZCS is significantly greater than that of CN and ZCS,

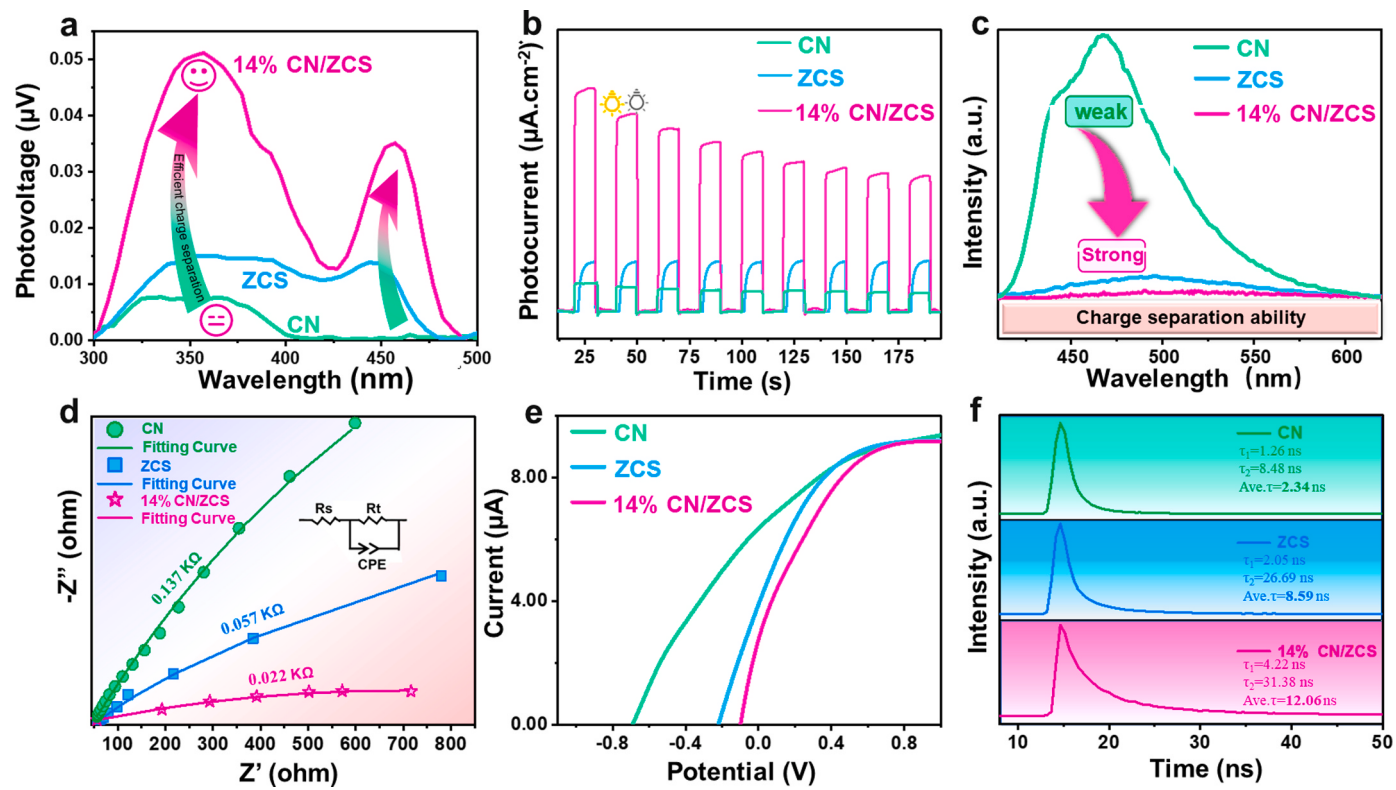


Fig. 7. (a) SPV spectra, (b) transient photocurrent responses, (c) PL spectra, (d) EIS Nyquist plots, (e) LSV spectra and (f) TRPL decay spectra of CN, ZCS and 14 % CN/ZCS.

unmasking the more expedited photocarriers separation efficiency. This result is supported by the photocurrent response (Fig. 7b) and the photoluminescence (PL) spectroscopy (Fig. 7c). The superior photocurrent density and lower PL emission peak of 14 % CN/ZCS unmask the positive role of built-in electric field for restricting the recombination of photocarriers. In addition, the electrochemical impedance spectroscopy (EIS) test (Fig. 7d) and linear scan voltammetry (LSV) (Fig. 7e) were carried out to surveillance the electron migration impedance and current density. In contrasted, the diameter of CN is bigger than that of 14 % CN/ZCS, demonstrating the constructed of heterojunction can reduce the interfacial charge transfer resistance, which is beneficial to photo-generated carrier transfer. This conclusion is further attested by the higher current density in the LSV spectrum. The time-resolved photoluminescence (TRPL) is calculated by applying the fitting the time-resolved PL decay curves (Fig. 7f). Compared with CN and ZCS, 14 % CN/ZCS unveil the longer intensity-average (τ) PL lifetime (12.06 ns), which implies that more electrons and $\bullet\text{O}_2$ can transfer to the surface of photocatalyst to engage oxidation and reduction reactions. Comprehensively, S-type charge transfer pathways structured by band structure matching play a crucial role in extending photogenerated electron lifetime for generating more $\bullet\text{O}_2$ and improving oxidation and reduction capabilities.

3.4. Reaction pathway and toxicity analysis

To identify the degradation pathway of the CIP and the reduction products of Cr (VI) over 14 % CN/ZCS in composite system, liquid chromatography mass spectrometer (LC-MS) and XPS were conducted. XPS survey spectrum of 14 % CN/ZCS after the reaction verifies the existence of Cr atoms on the surface of 14 % CN/ZCS (Fig. S11a), in contrast to the original photocatalyst. Cr 2p peaks are discovered at 577.3 eV and 586.6 eV, which are attributed to Cr (III) [33]. The peaks of Cr (VI) are not found, demonstrating that Cr (VI) is completely reduced (Fig. S11b). According to the LC-MS analysis (Fig. S12a-f), a

plausible degradation pathway of CIP was presented in Fig. 8a. In the pathway 1, the piperazinyl group is assaulted by $\bullet\text{O}_2$ and h^+ , leading to the oxidation of the CIP (m/z 332) to form H (m/z 362). Next, following by the oxidation of two formyl groups of product H, two products containing I (m/z 334) and J (m/z 334) are generated with further oxidation, the quinolone ring is further broken, and intermediate K (m/z 332) and L (m/z 226) is further broken down other small molecules and mineralized to form H_2O and CO_2 [34]. In the pathway 2, $\bullet\text{O}_2$ and h^+ play a pivotal role. The piperazine ring is initially assaulted, resulting in the production of B (m/z 362), next -CO is removed to transform C or D (m/z 334) [35]. In the pathway 3, the piperazine side chain undergoes progressive oxidative degradation induced by $\bullet\text{OH}$ attack on the piperazine ring. Amide B (m/z 362) is the first material of the ring opening during the piperazine oxidative process. Product C (m/z 334) is proposed because the missing of -CO group in the piperazinyl rings broken procedure. Then the C (m/z 334) is converted into E (m/z 306) due to the formylation of C (m/z 334) and further terminal oxidation produced F (m/z 263) [36,37]. Subsequently, F (m/z 263) conversion to G (m/z 204) through loss of the amino group. Eventually, original CIP molecules and intermediates are mineralized into other small molecules or CO_2 and H_2O .

Toxicity changes during CIP degradation can be predicted by the toxicity analysis software EPI. As displayed in Fig. 8b, the calculated acute toxicity of the product to fish and daphnia (LC_{50}) are 2.37×10^5 and $3.30 \times 10^5 \text{ mg/L}$, whereas that of green algae is $1.21 \times 10^5 \text{ mg/L}$. Simultaneous, chronic toxicity values (ChVs) of the product are 8.55×10^3 , 1.97×10^3 , and $1.50 \times 10^3 \text{ mg/L}$, respectively [38]. In pathway 1 and 3, the toxicity of the I, J and F incline to rise, but the toxicity of K, L and G decline dramatically as the reaction proceeded. In pathway 2, the toxicity of the products of CIP tend to steady, they consistently remain within the harmless range. Accordingly, during the CIP removal process, the 14 % CN/ZCS photocatalyst may produce some hazardous intermediates. Nevertheless, the reactive free radicals can disrupt and convert them into H_2O and CO_2 within an adequate

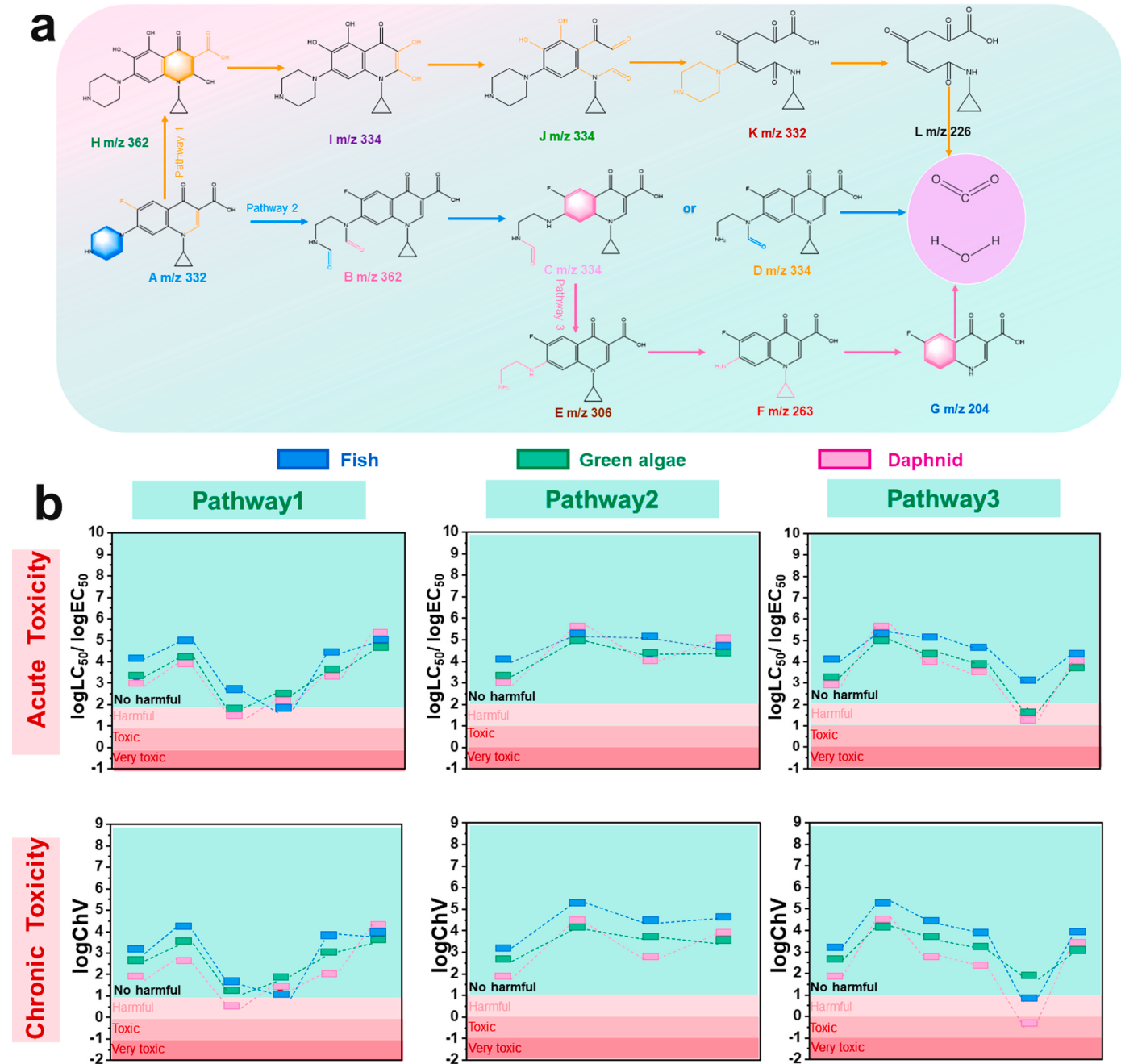


Fig. 8. (a) The possible degradation process of CIP by the 14 % CN/ZCS. (b) Evolution of the acute and chronic toxicity of CIP and its degradation intermediates to three aquatic organisms.

timeframe, justifying that the composite is extremely valid at degrading CIP. Consequently, it is evident that utilization of 14 % CN/ZCS catalyst does not have a negative impact on the environment, and thus, it can be considered a green, non-toxic, and non-polluting photocatalyst.

The excellent removal of complex contamination of 14 % CN/ZCS encouraged us to further investigate at the device level. Fig. 9a and b display the flow graphs of the wastewater treatment for the 14 % CN/ZCS catalyst actual application. Considering that the high diversity of catalysts in solution impacts reuse and may result in secondary contamination, polyurethane sponges were selected as loading devices, and catalysts sponges (namely CS) were made by impregnation method. The CS is loose and porous (Fig. 9c and d), and the catalyst is firmly attached to the sponge to ensure that it will not shed during the catalytic reaction. As present in Fig. 9e, the EDS-mapping image clearly show that

C, N, Zn, Cd, and S are homogeneously distributed in sponge, further evidence that the catalyst is successfully loaded onto the sponge. To test the performance of CS, we added Cr (VI) and CIP to secondary effluent from the Hebei university of technology wastewater treatment facility and used the removal rate of both as an indicator. The long-term stability was assessed by constant operation 40 h. The CS system continuously remove of complex contaminants from the wastewater without the need to wash the catalyst after a single reaction. The CS system can maintain 100 % Cr (VI) and 87.4 % CIP removal efficiency after completion of a single reaction (Fig. 9f). Noteworthy, the removal rate of the composite pollution remains above 70 % after 40 h of operation (Fig. 9g). Another strength is that the system sustains a satisfactory total organic carbon (TOC) removal rate after 8 h operation (Fig. 9h). Noteworthy, the increase in TOC removal in the reactor is probably due to the increase in

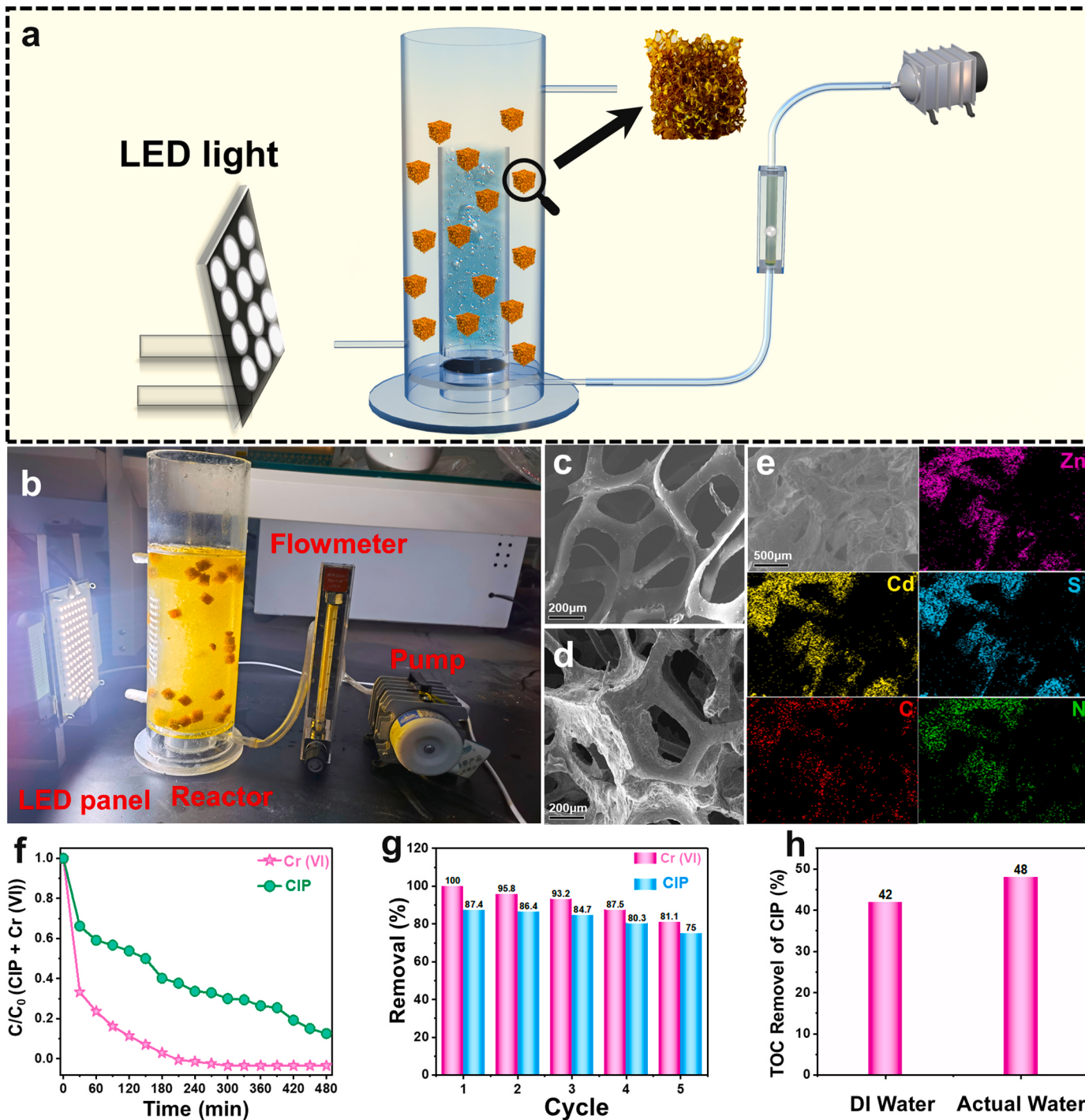


Fig. 9. (a) Design of actual water reaction devices. (b) Photograph of the wastewater treatment reaction devices. (c) Sponge. (d) Sponge after catalyst loading. (e) EDS elemental mappings. (f) Photocatalytic performance testing in reaction devices. (g) Cycle stability of 14 % CN/ZCS in reaction devices. (h) TOC removal rates in actual and deionized water bodies.

•O₂ as a result of the slight increase in oxygen concentration due to constant aeration. The above results indicate that our catalysts have a wide scope of practical applications.

4. Conclusions

In summary, S-scheme junctions consisting of Zn_{0.78}Cd_{0.22}S nanoparticles and g-C₃N₄ ultra-thin nanosheet were facilely manufactured through hydrothermal method. Noteworthy, the combination of Zn_{0.78}Cd_{0.22}S with g-C₃N₄ can effectively extend the electronic life and

generated more •O₂. In addition, DFT calculations show that electric field within a S-heterojunction decreases the electrochemical impedance and enhanced the electron transfer, thereby extending the lifetime of photogenerated charge carriers. Further experimental results justify that •O₂ plays a role in both oxidation and reduction processes and composites display excellent photocatalytic properties, and 88.6 % of CIP and 100 % of Cr (VI) can be simultaneously removed and the photocatalytic removal efficiency of the composite system is superior to the single system. This can be attributed to the fact that CIP and Cr (VI) act as h⁺ and e⁻ scavengers to produce more •O₂ and •OH. Moreover, the

CN/ZCS with excellent photocatalytic activity and great stability also show promising application potential in practice. This work will have an impact on the design and development of sulfides-based S-scheme photocatalysts with enhanced electronic lifetime and photocatalytic activity for removal of complex contamination.

CRediT authorship contribution statement

Kang Wang: Investigation, Writing – original draft and Formal analysis. **Shuming Zeng:** Software. **Geng Li:** Software. **Yilin Dong:** Validation. **Qiuwen Wang:** Investigation. **Lijun Zhang:** Original Draft. **Zhijun Ren:** Supervision and Funding acquisition. **Pengfei Wang:** Supervision, Funding acquisition and Writing – review & editing.

Declaration of Competing Interest

The authors declare that they have no known competing financial interests or personal relationships that could have appeared to influence the work reported in this paper.

Data availability

The authors do not have permission to share data.

Acknowledgements

The authors gratefully acknowledge the financially support by the National Natural Science Foundation of China as general projects (grant No. 42277059 and 22006029), Tianjin Commission of Science and Technology as Key Technologies R&D Projects (21YFSNSN00250), Doctoral Innovation Project of Hebei Province (CXZZBS2023031).

Appendix A. Supporting information

Supplementary data associated with this article can be found in the online version at doi:10.1016/j.apcatb.2023.123565.

References

- [1] S. Zhang, H. Lan, Y. Cui, X. An, H. Liu, J. Qu, Insight into the key role of Cr intermediates in the efficient and simultaneous degradation of organic contaminants and Cr (VI) reduction via g-C₃N₄-assisted photocatalysis, Environ. Sci. Technol. 56 (2022) 3552–3563.
- [2] W. Yan, Y. Xiao, W. Yan, R. Ding, S. Wang, F. Zhao, The effect of bioelectrochemical systems on antibiotics removal and antibiotic resistance genes: a review, Chem. Eng. J. 358 (2019) 1421–1437.
- [3] X. He, Y. Xu, J. Chen, J. Ling, Y. Li, L. Huang, X. Zhou, L. Zheng, G. Xie, Evolution of corresponding resistance genes in the water of fish tanks with multiple stresses of antibiotics and heavy metals, Water Res. 124 (2017) 39–48.
- [4] Y. Zhu, W. Fan, T. Zhou, X. Li, Removal of chelated heavy metals from aqueous solution: a review of current methods and mechanisms, Sci. Total Environ. 678 (2019) 253–266.
- [5] Z.H. Diao, X.R. Xu, D. Jiang, J.J. Liu, L.J. Kong, G. Li, L.Z. Zuo, Q.H. Wu, Simultaneous photocatalytic Cr(VI) reduction and ciprofloxacin oxidation over TiO₂/Fe⁰ composite under aerobic conditions: performance, durability, pathway and mechanism, Chem. Eng. J. 315 (2017) 167–176.
- [6] C. Liu, P. Wang, Y. Qiao, G. Zhou, Self-assembled Bi₂SeO₅/rGO/MIL-88A Z-scheme heterojunction boosting carrier separation for simultaneous removal of Cr (VI) and chloramphenicol, Chem. Eng. J. 431 (2022), 133289.
- [7] L. Lu, J. Liu, Z. Li, X. Zou, J. Guo, Z. Liu, J. Yang, Y. Zhou, Antibiotic resistance gene abundances associated with heavy metals and antibiotics in the sediments of Changshou Lake in the three Gorges Reservoir area, China, Ecol. Indic. 113 (2020), 106275.
- [8] L. Chandana, B. Lakshminarayana, C. Subrahmanyam, Influence of hydrogen peroxide on the simultaneous removal of Cr(VI) and methylene blue from aqueous medium under atmospheric pressure plasma jet, J. Environ. Chem. Eng. 3 (2015) 2760–2767.
- [9] W. Li, S. Yang, W. Wang, Q. Liu, J. He, B. Li, Z. Cai, N. Chen, H. Fang, S. Sun, Simultaneous removal of Cr(VI) and acid orange 7 from water in pyrite-persulfate system, Environ. Res. 189 (2020), 109876.
- [10] J. Ding, Y. Tang, S. Zheng, S. Zhang, H. Xue, Q. Kong, H. Pang, The synthesis of MOF derived carbon and its application in water treatment, Nano Res. 15 (2022) 6793–6818.
- [11] L.P. Zhang, Z. Liu, X.L. Zhou, C. Zhang, Q.W. Cai, R. Xie, X.J. Ju, W. Wang, Y. Faraj, L.Y. Chu, Novel composite membranes for simultaneous catalytic degradation of organic contaminants and adsorption of heavy metal ions, Sep. Purif. Technol. 237 (2020), 116364.
- [12] Y. Hu, Y. Jin, P. Zhang, Y.-n Zhang, G. Zhao, Efficient removal of bisphenol A and Cr(VI) simultaneously in an advanced redox photoelectrocatalytic system over dual 3D TiO₂ photoelectrodes, Appl. Catal. B Environ. 322 (2023), 122102.
- [13] J. Niu, R. Hu, L. Tang, Y. Huang, J. Cheng, Y. Hu, In-situ growth of C-F@CCS@ZIF8/67-1/1 photocatalysts with internal electric field and interfacial enhancement on cobalt-copper foam surface for simultaneous removal of ciprofloxacin and Cr(VI), Appl. Catal. B Environ. 334 (2023), 122857.
- [14] B. Peng, Y. Lu, J. Luo, Z. Zhang, X. Zhu, L. Tang, L. Wang, Y. Deng, X. Ouyang, J. Tan, J. Wang, Visible light-activated self-powered photoelectrochemical aptasensor for ultrasensitive chloramphenicol detection based on DFT-proved Z-scheme Ag₂CrO₄/g-C₃N₄/graphene oxide, J. Hazard. Mater. 401 (2021), 123395.
- [15] H. Zhao, Q. Zhou, M. Li, R. Zhou, Y. Mao, P. Wang, Photocatalytic O₂ activation and reactive oxygen species evolution by surface B-N bond for organic pollutants degradation, Appl. Catal. B Environ. 310 (2022), 121329.
- [16] T.O. Ajiboye, O.A. Oyewo, D.C. Onwudiwe, Simultaneous removal of organics and heavy metals from industrial wastewater: a review, Chemosphere 262 (2021), 128379.
- [17] X. Zhao, J. Feng, J. Liu, W. Shi, G. Yang, G.C. Wang, P. Cheng, An efficient, visible-light-driven, hydrogen evolution catalyst NiS_xCd_{1-x}S nanocrystal derived from a metal–organic framework, Angew. Chem. 130 (2018) 9938–9942.
- [18] T. Zhang, F. Meng, Y. Cheng, N. Dewangan, G.W. Ho, S. Kawi, Z-scheme transition metal bridge of Co₃S₈/Cd/CdS tubular heterostructure for enhanced photocatalytic hydrogen evolution, Appl. Catal. B Environ. 286 (2021), 119853.
- [19] B. Wang, C. Chen, Y. Jiang, P. Ni, C. Zhang, Y. Yang, Y. Lu, P. Liu, Rational designing 0D/1D Z-scheme heterojunction on CdS nanorods for efficient visible-light-driven photocatalytic H₂ evolution, Chem. Eng. J. 412 (2021), 128690.
- [20] S. Cao, J. Low, J. Yu, M. Jaroniec, Polymeric photocatalysts based on graphitic carbon nitride, Adv. Mater. 27 (2015) 2150–2176.
- [21] T. Yan, H. Liu, Z. Jin, g-C₃N₄/α-Fe₂O₃ supported zero-dimensional Co₃S₄ nanoparticles form S-scheme heterojunction photocatalyst for efficient hydrogen production, Energy Fuels 35 (2020) 856–867.
- [22] Y. Wang, Y. He, Y. Chi, P. Yin, L. Wei, W. Liu, X. Wang, H. Zhang, H. Song, Construction of S-scheme pn heterojunction between protonated g-C₃N₄ and α-MnS nanosphere for photocatalytic H₂O₂ production and in situ degradation of oxytetracycline, J. Environ. Chem. Eng. 11 (2023), 109968.
- [23] H. Wang, Y. Su, H. Zhao, H. Yu, S. Chen, Y. Zhang, X. Quan, Photocatalytic oxidation of aqueous ammonia using atomic single layer graphitic-C₃N₄, Environ. Sci. Technol. 48 (2014) 11984–11990.
- [24] L. Li, D. Ma, Q. Xu, S. Huang, Constructing hierarchical ZnIn₂S₄/g-C₃N₄ S-scheme heterojunction for boosted CO₂ photoreduction performance, Chem. Eng. J. 437 (2022), 135153.
- [25] P. Xia, S. Cao, B. Zhu, M. Liu, M. Shi, J. Yu, Y. Zhang, Designing a 0D/2D S-scheme heterojunction over polymeric carbon nitride for visible-light photocatalytic inactivation of bacteria, Angew. Chem. Int. Ed. 59 (2020) 5218–5225.
- [26] M. Tan, Y. Ma, C. Yu, Q. Luan, J. Li, C. Liu, W. Dong, Y. Su, L. Qiao, L. Gao, Boosting photocatalytic hydrogen production via interfacial engineering on 2D ultrathin Z-scheme ZnIn₂S₄/g-C₃N₄ heterojunction, Adv. Funct. Mater. 32 (2022), 2111740.
- [27] Z. Zhu, H. Huang, L. Liu, F. Chen, N. Tian, Y. Zhang, H. Yu, Chemically bonded α-Fe₂O₃/Bi₄Mo₈Cl dot-on-plate Z-scheme junction with strong internal electric field for selective photo-oxidation of aromatic alcohols, Angew. Chem. Int. Ed. 61 (2022), e202203519.
- [28] S. Li, M. Cai, Y. Liu, C. Wang, R. Yan, X. Chen, Constructing Cd_{0.5}Zn_{0.5}S/Bi₂WO₆ S-scheme heterojunction for boosted photocatalytic antibiotic oxidation and Cr (VI) reduction, Adv. Powder Mater. 2 (2023), 100073.
- [29] Q. Zhang, J. Chen, X. Gao, H. Che, P. Wang, Y. Ao, In-depth insight into the mechanism on photocatalytic synergistic removal of antibiotics and Cr (VI): the decisive effect of antibiotic molecular structure, Appl. Catal. B Environ. 313 (2022), 121443.
- [30] G.R. Eaton, S.S. Eaton, D.P. Barr, R.T. Weber, Quantitative Epr, Springer Science & Business Media, 2010.
- [31] Y. Dong, D. Xu, Q. Wang, G. Zhang, Q. Zhang, Z. Zhang, L. Lv, Y. Xia, Z. Ren, P. Wang, Tailoring the electronic structure of ultrathin 2D Bi₃O₄Cl sheets by boron doping for enhanced visible light environmental remediation, Appl. Surf. Sci. 542 (2021), 148521.
- [32] H. Yaghoubi, Z. Li, Y. Chen, H.T. Ngo, V.R. Bhethanabotla, B. Joseph, S. Ma, R. Schlaf, A. Takshi, Toward a visible light-driven photocatalyst: the effect of midgap states-induced energy gap of undoped TiO₂ nanoparticles, ACS Catal. 5 (2015) 327–335.
- [33] F. Yuan, Z. Sun, C. Li, Y. Tan, X. Zhang, S. Zheng, Multi-component design and in-situ synthesis of visible-light-driven SnO₂/g-C₃N₄/diatomite composite for high-efficient photoreduction of Cr(VI) with the aid of citric acid, J. Hazard. Mater. 396 (2020), 122694.
- [34] C.-H. Shen, X.-J. Wen, Z.-H. Fei, Z.-T. Liu, Q.-M. Mu, Visible-light-driven activation of peroxymonosulfate for accelerating ciprofloxacin degradation using CeO₂/Co₃O₄ p-n heterojunction photocatalysts, Chem. Eng. J. 391 (2020), 123612.
- [35] Z. Wang, X. Cai, X. Xie, S. Li, X. Zhang, Z. Wang, Visible-LED-light-driven photocatalytic degradation of ofloxacin and ciprofloxacin by magnetic biochar modified flower-like Bi₂WO₆: the synergistic effects, mechanism insights and degradation pathways, Sci. Total Environ. 764 (2021), 142879.
- [36] Z.-H. Diao, X.-R. Xu, D. Jiang, G. Li, J.-J. Liu, L.-J. Kong, L.-Z. Zuo, Enhanced catalytic degradation of ciprofloxacin with FeS₂/SiO₂ microspheres as

heterogeneous Fenton catalyst: kinetics, reaction pathways and mechanism, *J. Hazard. Mater.* 327 (2017) 108–115.

[37] M.S. Yahya, N. Oturan, K. El Kacemi, M. El Karbane, C. Aravindakumar, M. A. Oturan, Oxidative degradation study on antimicrobial agent ciprofloxacin by electro-Fenton process: kinetics and oxidation products, *Chemosphere* 117 (2014) 447–454.

[38] W. Gao, G. Li, Q. Wang, L. Zhang, K. Wang, S. Pang, G. Zhang, L. Lv, X. Liu, W. Gao, L. Sun, Y. Xia, Z. Ren, P. Wang, Ultrathin porous Bi₂WO₆ with rich oxygen vacancies for promoted adsorption-photocatalytic tetracycline degradation, *Chem. Eng. J.* 464 (2023), 142694.